Available online at www.sciencedirect.com

ScienceDirect

Procedia Manufacturing 53 (2021) 213–222

Procedia MANUFACTURING

www.elsevier.com/locate/procedia

49th SME North American Manufacturing Research Conference, NAMRC 49, Ohio, USA

Contributions of scanning metrology uncertainty to milling force prediction

[a]Timothy No, [a,b]Michael Gomez, [a,b]Tony Schmitz*

[a]*University of Tennessee, Knoxville, TN, 37996, USA*
[b]*Manufacturing Science Division, Oak Ridge National Laboratory, Oak Ridge, TN, 37831, USA*

* Corresponding author. Tel.: +1-865-974-6141; fax: +1-865-974-5274. *E-mail address:* tony.schmitz@utk.edu

Abstract

This paper describes an uncertainty evaluation for axial location-dependent cutting edge radius and angle values extracted from structured light scans of a variable pitch endmill. Two cases are evaluated: 1) a single scan of the endmill is performed and that scan is manually fit five times to record the cutting edge geometry for all teeth on the endmill; and 2) five scans of the endmill are performed and each scan is manually fit a single time. Both cases therefore include five manual fits. The standard deviations in radius and angle values are used to represent the statistical uncertainty and the two cases are compared. The mean standard deviations in radius are 0.005 mm and 0.007 mm; the mean standard deviations in angle are 0.066 deg and 0.092 deg. As expected, the uncertainties are higher with additional scans. The scan results are then used in a time-domain simulation to predict the cutting force profiles for the variable pitch endmill. It is shown that the two cases provide similar agreement between prediction and measurement due to the small measurement uncertainties.

Keywords: Milling; force; modeling; uncertainty; structured light

1. Introduction

Machining is a key manufacturing capability both as a standalone application and as a complement to additive manufacturing. For the latter hybrid manufacturing scenario, machining follows additive pre-form deposition to produce final surface finish and selected features (e.g., mating surfaces and tapped holes). One key capability to predict and monitor machining process performance is dynamic force prediction and measurement. The time-dependent milling force signal contains information about process stability (forced vibration versus self-excited vibration), tool wear (force growth until tool failure), runout (varying chip load), and surface location error (part geometry errors due to forced vibrations), to name a few [1-2]. Primary considerations include the endmill's cutting edge geometry, the cutting force model that relates the tangential and normal force components to the chip geometry (thickness and width), and the frequency response function at the tool tip, which includes contributions from the endmill, holder, spindle, and machine.

In recent work, the authors have implemented scanning metrology to model the performance of endmills during machining without requiring a model of the tool geometry from the manufacturer. Structured light, or fringe, projection was applied to collect point clouds from the complex endmill surfaces. The measurements proceeded by first preparing the endmill surface using a removable anti-glare coating and attaching reference targets to the shank surface to enable multiple measurements to be stitched together and generate the solid model. Second, multiple scans were completed to obtain

[*] Notice: This manuscript has been authored by UT-Battelle, LLC, under contract DE-AC05-00OR22725 with the US Department of Energy (DOE). The US government retains and the publisher, by accepting the article for publication, acknowledges that the US government retains a nonexclusive, paid-up, irrevocable, worldwide license to publish or reproduce the published form of this manuscript, or allow others to do so, for US government purposes. DOE will provide public access to these results of federally sponsored research in accordance with the DOE Public Access Plan (http://energy.gov/downloads/doe-public-access-plan).

10.1016/j.promfg.2021.06.024

the full point cloud and 3D model [3-6]. Once the cutting edge coordinates were extracted, they were used in a time domain simulation to predict the dynamic cutting force as a function of the machining parameters and a mechanistic cutting force model. The focus was non-standard cutting edge geometries since detailed information may not be available for proprietary designs.

Nomenclature

r	radius of point on endmill cutting edge
ϕ	angle of point on endmill cutting edge
z	position along endmill axis
$\Delta\phi$	angular resolution in time domain simulation
SR	steps per revolution in time domain simulation
RO	runout for point on endmill cutting edge
F_t	tangential component of cutting force
F_n	normal component of cutting force
k_{tc}	cutting force coefficient for tangential component
k_{nc}	cutting force coefficient for normal component
k_{te}	edge effect force coefficient for tangential component
k_{ne}	edge effect force coefficient for normal component
m	modal mass
c	modal viscous damping coefficient
k	modal stiffness
x	feed direction for milling operation
y	perpendicular direction to x in the cut plane
F_x	x component of cutting force
F_y	y component of cutting force

Other authors have studied non-standard geometries as well. Wang and Yang [7] presented force models for a cylindrical roughing endmill with sinusoidal cutting edges. Merdol and Altintas [8] modeled the serration profile by fitting points along a cubic spline projected on the helical flutes. This geometric model was used to generate a time domain milling model. Dombovari *et al.* [9] used the semi-discretization method to analyze the stability of serrated endmills. Later, he and others created general models for various tool geometries [10-11]. Koca and Budak [12] used a linear edge-force model and the semi-discretization method for force and stability modeling and optimized the serration waveform shape to reduce milling forces and increase stability. Grabowski *et al.* [13] extended their mechanistic model to calculate the process forces of serrated endmills. Tehranizadeh and Budak [14] proposed a genetic algorithm to optimize the design of serration shapes.

Researchers have also evaluated the measurement uncertainty for scanning systems. Mahmud *et al.* studied a plane laser sensor mounted on the ram of a coordinate measuring machine (CMM). They considered the angle of incidence between the optical plane and the scanned surface, the scanning path, and the analysis of the resulting point cloud [15]. Müller *et al.* examined the influence of test specimen surface properties on structured light scanning measurements. They showed that the color of polymer gear wheels affected the measurement and corresponding uncertainties [16-17]. Polo *et al.* measured steel gage blocks with two different structured light scanners at different resolutions and compared the uncertainties [18]. Adamczyk *et al.* studied the effects of ambient temperature changes on structured light scanners and proposed a compensation scheme [19]. Kaszynski *et al.* described a reverse engineering process for integral blade rotors (IBRs) using structured light scanning [20]. A calibration block was used to evaluate uncertainty. Rosman *et al.* showed how adaptive pattern selection can maximize information gain for structured light scanning [21]. Jain *et al*. presented a methodology to estimate the instrument transfer function for a commercial structured light scanner and its uncertainty [22].

This paper builds on previous efforts by studying the propagation of uncertainty in the cutting edge geometry obtained from structured light scanning to the predicted, time-dependent cutting force in milling. A variable pitch (i.e., non-uniform tooth spacing), five helical tooth, solid carbide, bull nose endmill was selected for geometric measurements and cutting tests. However, the approach can be extended to any endmill geometry, including square, ball nose, bull nose, variable radius, variable helix, and indexable endmill designs.

The paper is organized as follows. In section 2, the structured light scanning approach is described and results are presented, including uncertainties arising from manual edge identification and multiple scans of the same endmill. In section 3, the time domain simulation is detailed. In section 4, the experimental setup for milling trials is provided. In section 5, a comparison of measured and simulated forces is presented including variations in the simulated time-dependent force profiles due to uncertainty in the cutting edge geometry. Finally, conclusions are provided in section 6.

2. Structured light scanning and uncertainty

In structured light, or fringe, projection, a common approach is to project a pattern of parallel lines onto the surface under test. Because the reflected lines are distorted due to the surface geometry, the measurement system can use the relative positions of the projector and one or more cameras (two cameras is typical) together with the distorted lines to reconstruct the three-dimensional surface. Because the approach only provides line of sight data, multiple scans are completed for various part orientations and stitched together to define the full three-dimensional surface geometry. While many commercial options are available, the GOM ATOS Capsule system was used for this research.

The measurements proceeded by first preparing the endmill surface using a removable anti-glare (*i*-PrOH TiO_2) coating and attaching reference targets to the shank surface to enable multiple measurements to be stitched together and generate the solid model; a photograph is provided in Fig. 1. Multiple scans were then completed to obtain the point cloud and 3D model.

The procedure used to extract the edge coordinates from the solid model included four steps.

1. Using the best fit cylinder to the tool shank and the fluted end's extreme point, the origin was established on the tool's center line (see top center in Fig. 2).
2. The points located on the five helical cutting edges were selected. This step required manual manipulation within the GOM software (see black/green symbols in Fig. 2).
3. The radius, r, and angle, ϕ, for each black/green edge point in Fig. 2was calculated. The teeth angles were normalized

to a selected tooth and constrained to values between 0 and 360 deg; the z value was retained to obtain a triplet, {r, ϕ, z} for each point.

4. Because the point density was higher than required for the time domain simulation and the point spacing was not uniform, linear interpolation was used to obtain the triplet for axial (z) slices located every 0.1 mm over the full flute length; see Fig. 2, which shows the solid model with edge points.

Fig. 1. Tool preparation for structured light scanning. (Left) variable pitch endmill. (Right) application of *i*-PrOH TiO_2 coating and reference targets.

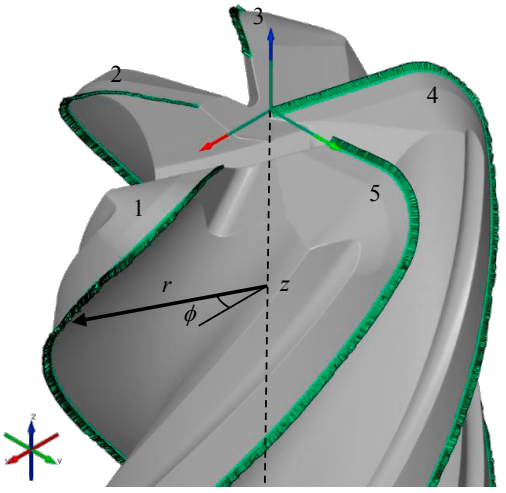

Fig. 2. Solid model for variable pitch endmill.

Example angle results are provided in Fig. 3 for a single scan with manual identification of the five cutting edges. In this figure, unwrapping the cylindrical tool surface onto the cartesian coordinate system yields straight lines for the helical cutting edges. By modifying the horizontal axis to be the product of radius and angle, the helix angle for all five teeth was determined to be 37.9 deg.

The angles between the teeth are obtained by differencing the points on adjacent edges at each z location from Fig. 3. These reports are displayed in Fig. 4. It is observed that the average angle between teeth 1 and 2 is 68.1 deg, the average angle between teeth 2 and 3 is 77.0 deg, the average angle between teeth 3 and 4 is 72.1 deg, the average angle between teeth 4 and 5 is 66.9 deg, and the average angle between teeth 5 and 1 is 75.9 deg. This geometry can be compactly represented as 68-77-72-67-76 deg for the variable pitch endmill. The teeth spacing for a proportional pitch endmill with five teeth is 72 deg, so the departures from nominal are: (-4)-(+5)-(0)-(-5)-(+4) deg. In this representation, a negative value indicates that the adjacent teeth are more closely spaced than nominal and vice versa.

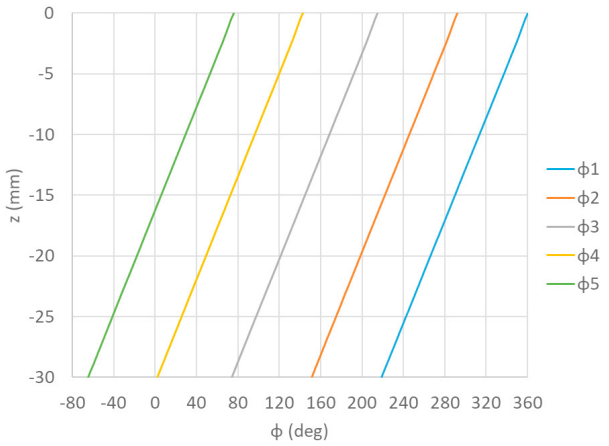

Fig. 3. Angles, ϕ, for points on five cutting edges (1-5) as a function of axial location, z.

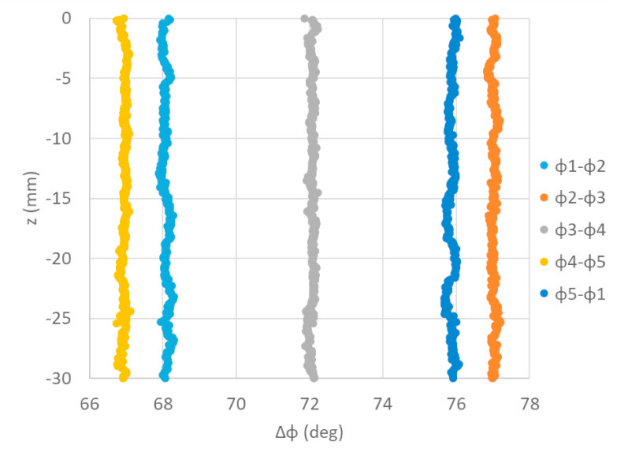

Fig. 4. Pitch angles, $\Delta\phi$, between the five cutting edges (1-5) as a function of axial location, z.

Figure 5 displays example radius results, where the horizontal scale is dominated by the bull nose radius. The average corner radius for all five teeth is 3.03 mm; the individual values are: {2.97, 3.07, 3.03, 3.04, and 3.03} mm for tooth 1 to tooth 5. The scale is modified in Fig. 6 to exclude the bull nose and highlight the variation in radii between the five teeth. The average radii from z = -3 mm to -30 mm for the five teeth are: {9.46, 9.46, 9.47, 9.47, and 9.47} mm.

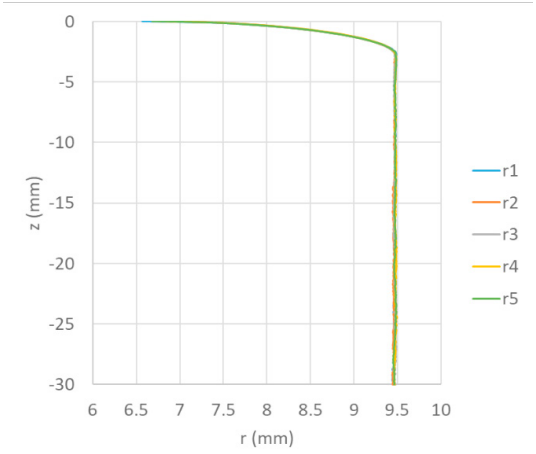

Fig. 5. Radii, r, for points on five cutting edges (1-5) as a function of axial location, z. The bull nose is located at the tool tip (z = 0 to -3 mm).

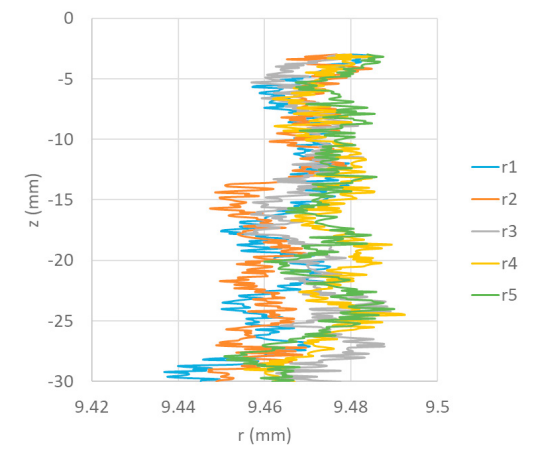

Fig. 6. Radii, r, for points on five cutting edges (1-5) as a function of axial location, z. The bull nose portion from Fig. 5 is excluded.

The single scan-single manual fit data presented in Figs. 3-6 enabled the endmill geometry to be identified. However, it did not yield information about the uncertainty in the edge geometry measurement. Following the Type A (statistical) uncertainty evaluation described in NIST Technical Note 1297 [23], the uncertainty contributed by the manual edge identification process was first evaluated. To quantify the associated variation, a single scan was performed and the five cutting edges were manually identified five times each from that single scan by one software user. The standard deviations in the angle and radius at each z location (0.1 mm intervals) for each of the five teeth were then calculated. These standard deviations were taken to represent the uncertainties due to manual fitting. The results are displayed in Figs. 7 (angle) and 8 (radius), where the ball nose geometry was again excluded.

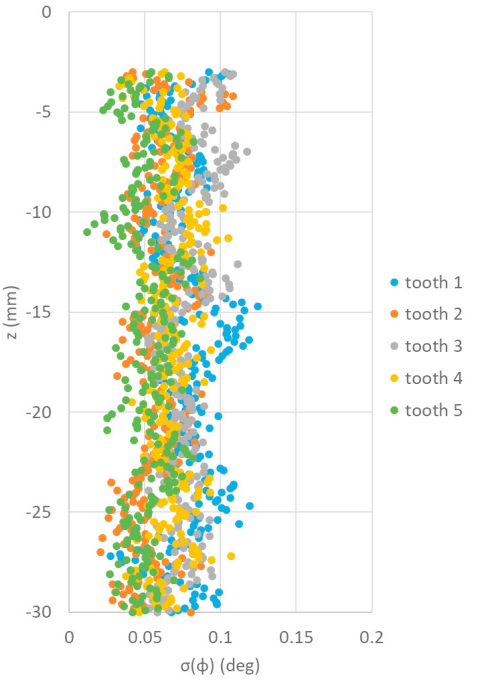

Fig. 7. Standard deviation, σ, in z-dependent cutting edge angles, ϕ, for five manual fits of a single scan (measurement).

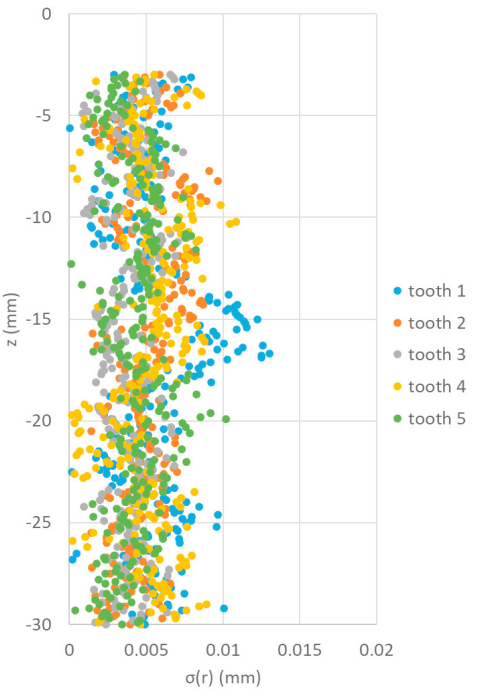

Fig. 8. Standard deviation, σ, in z-dependent cutting edge radii, r, for five manual fits of a single scan (measurement).

Second, the uncertainty contribution due to scanning was included. The added uncertainty from the scan non-repeatability was assessed by performing five scans of the end mill and completing a single manual fit of the five cutting edges for each scan. The logic is that, if the scan repetitions contributed no additional uncertainty, then the standard deviation profile would be similar to the five fit-single scan case since both cases included five manual fits. However, if the scan repeats contributed additional uncertainty, then the standard deviations would increase. While it is not possible to isolate the scan uncertainty independently since the manual fit is required to identify the measurand, or cutting edge geometry, this approach does enable the increase in uncertainty to be identified.

The z-dependent standard deviations for cutting edge angles and radii are displayed in Figs. 9 and 10 for five scans with one fit (of all five teeth) for each scan. It is observed that both the mean values and ranges increase for angles and radii over the five fit-single scan results in Figs. 7 and 8.

To provide a more compact visual comparison of the distributions in angle standard deviations between Fig. 7 (five fits for one scan) and Fig. 9 (one fit for each of five scans), the two histograms in Fig. 11 are presented (20 bins for each histogram). These show the distribution in all standard deviations for all five teeth at all z locations. It is clear that the mean and range increase with the additional scans. Similar results are observed in Fig. 12 for the radii.

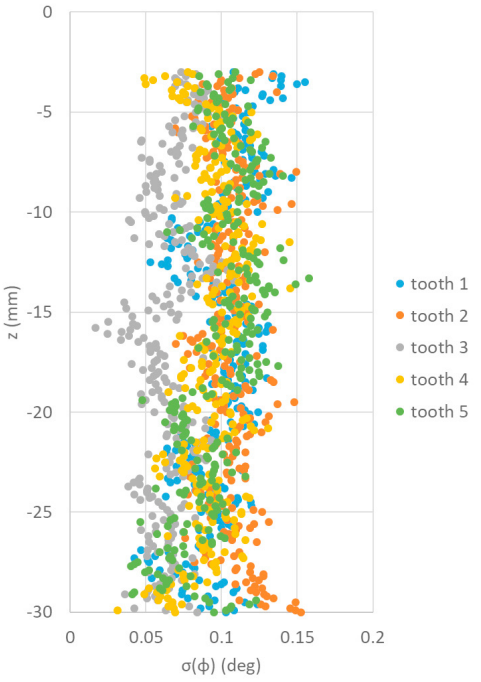

Fig. 9. Standard deviation, σ, in z-dependent cutting edge angles, ϕ, for one manual fit each of five scans.

To enable a numerical comparison between the histograms, the mean and standard deviation were calculated for each. This represents an unusual situation because the values are: 1) the mean of the standard deviations in the histograms; and 2) the standard deviation of the standard deviations in the histograms. The results are presented in Table 1. The percent increases from single scan to five scans (both with five independent manual fits) are: 1) angle mean = (0.092 – 0.066)/0.066*100 = 39.4%; 2) angle standard deviation = 27.8%; 3) radius mean = 40%; and 4) radius standard deviation = 50%. Clearly, the scan non-repeatability is an important contributor to the overall uncertainty in identifying the cutting edge coordinates, but less than the manual fitting. If their contributions were equal, a 100% increase would be anticipated.

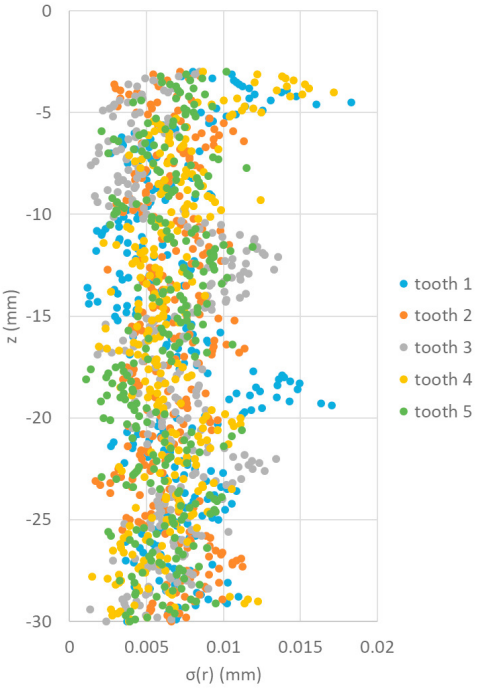

Fig. 10. Standard deviation, σ, in z-dependent cutting edge radii, r, for one manual fit each of five scans.

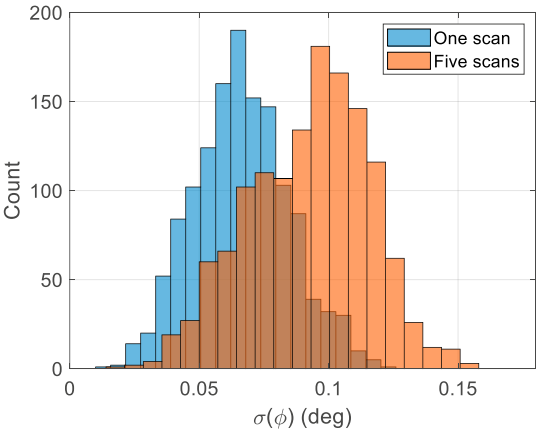

Fig. 11. Histogram of standard deviations, σ, in cutting edge angles, ϕ, for five manual fits of one scan (all five teeth, all z values) and single fits of five scans.

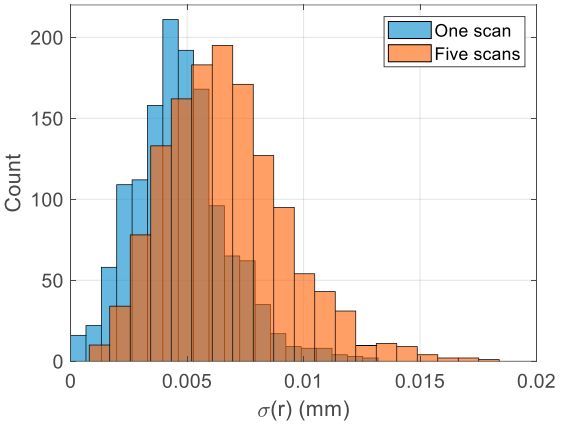

Fig. 12. Histogram of standard deviations, σ, in radii, r, for five manual fits of one scan (all five teeth, all z values) and single fits of five scans.

Table 1. Numerical analysis of histograms in Figs. 11 and 12.

Case	Measure	Mean of σ	Std. dev. of σ
Five fits of single scan	Angle	0.066 deg	0.018 deg
One fit of five scans	Angle	0.092 deg	0.023 deg
Five fits of single scan	Radius	0.005 mm	0.002 mm
One fit of five scans	Radius	0.007 mm	0.003 mm

3. Time domain simulation

Time domain simulation enables numerical solution of the coupled, time-delay equations of motion for milling in small time steps [1]. It is well suited to incorporating the inherent complexities of milling dynamics, including the nonlinearity that occurs if the tooth leaves the cut due to large amplitude vibrations and complicated tool geometries. The simulation used in this study is described in the following paragraphs.

The time domain simulation has three special requirements: use the actual tooth angles, include the radius variation as runout, and incorporate the bull nose geometry. For the tooth angles, the measured angles from the scanned edge were arranged in an array, where the columns were the individual teeth and the rows were the z locations (in steps of 0.1 mm). These z locations extended over the entire cutting length, but the array was truncated to include rows only up to the commanded axial depth when the simulation was executed. This enables any axial depth to be simulated (up to the cutting length). A row array of closely spaced tooth angles for use in the time domain simulation was then defined. The resolution in this array was: $\Delta\phi = 360/SR$, where SR is the number of steps per revolution in the simulation.

Once this array was defined, the measured tooth angles were specified in an index array with each entry given by: round($\phi/\Delta\phi$), where ϕ is the measured angle of the tooth at the selected z location and round is the MATLAB function that rounds to the nearest integer value. This index array was then used to specify the angle of any tooth at any z location by identifying the nearest preselected value from the closely spaced tooth angle array for use in the simulation. The reason for this approach is that the current chip thickness in milling depends not only on the commanded chip thickness and current vibration, but also the surface left by the previous teeth at the current tooth angle. To be able to do so conveniently, this information must be organized according to specified tooth angles.

The tool's radius variation was included as runout, *RO*. The z-dependent *RO* values for each tooth were also arranged in an array, where the columns were the individual teeth and the rows were the z locations (again in steps of 0.1 mm). Note that a negative *RO* value reduces the chip thickness for the current tooth, but leaves behind material that the next tooth must remove (and therefore increases that chip thickness).

Two other data organization requirements were: 1) the surface that was left behind by the current tooth; and 2) the actual commanded chip thickness. To keep track of the previously machined surface, another array was defined that recorded the surface location in the tool's normal direction for each simulation time step. The columns of this matrix were the number of steps per revolution and the rows were the z locations. The influence of runout on subsequent chip thickness values was captured in this matrix.

Because there were small variations in the tooth angles from the nominal helix profile (Fig. 4), the commanded chip thickness was also modified to account for the actual tooth angle using the circular tooth path approximation. This approximation calculates the nominal chip thickness from the product of the feed per tooth and the sine of the tooth angle. Finally, the bull nose portion of the endmill was incorporated in the simulation by projecting the forces in the appropriate directions using the nose surface normal at each z location. Also, the axial depth was updated to account for the arc length on the nose radius [1].

Given this information, the simulation proceeded as follows:

1. 1. The instantaneous chip thickness, $h(t)$, was determined using the commanded chip thickness, runout, and vibration of the current and previous teeth at the selected tooth angle.
2. The cutting force components in the tangential, t, and normal, n, directions were calculated at each axial slice using:

$$F_t(t) = k_{tc} b h(t) + k_{te} b \quad (1)$$

$$F_n(t) = k_{nc} b h(t) + k_{ne} b \quad (2)$$

where b is the slice width (0.1 mm) and the cutting force coefficients are identified by the subscripts: t or n for direction; and c or e for cutting or edge effect. These forces were then summed over all axial slices engaged in the cut.

3. The summed force components were used to find the new displacements by numerical solution of the differential equations of motion in the x (feed) and y directions:

$$m_x \ddot{x} + c_x \dot{x} + k_x x = F_t(t)\cos\phi + F_n(t)\sin\phi \quad (3)$$

$$m_y \ddot{y} + c_y \dot{y} + k_y y = F_t(t)\sin\phi - F_n(t)\cos\phi \quad (4)$$

where m is the modal mass, c is the modal viscous damping coefficient, and k is the modal stiffness. The subscripts identify the direction and multiple degrees-of-freedom in each direction can be accommodated.

4. The tool rotation angle was incremented by adding one to each entry in the tooth angle index array and the process was repeated.

4. Experimental setup

The experimental setup for milling force measurement is shown in Fig. 13. Trials were completed on a Haas TM-1 three-axis computer numerically controlled (CNC) milling machine. The (wrought) titanium 6Al-4V workpiece was mounted on a cutting force dynamometer (Kistler 9257B) and the endmill was clamped in a collet holder and inserted in the CAT-40 spindle interface. Tests were performed at a 5 mm axial depth of cut and 1.91 mm radial depth (10% radial immersion for the 19.1 mm diameter endmill). The commanded feed per tooth for the down (climb) milling experiments ranged from 75 µm/tooth to 250 µm/tooth; the spindle speed was 960 rpm.

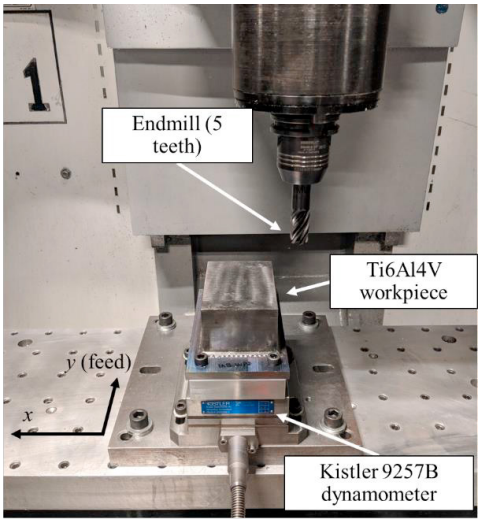

Fig. 13. Experimental setup for milling force measurement.

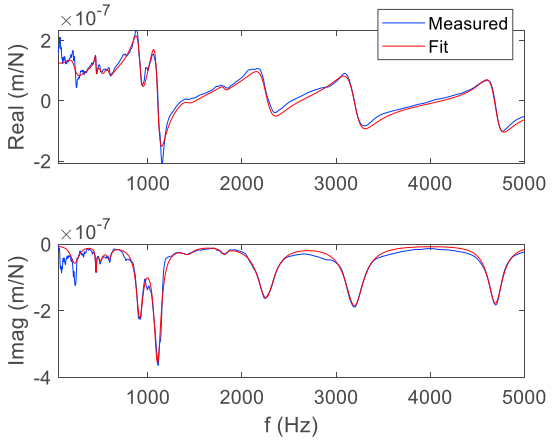

Fig. 14. Tool tip FRF for the x (feed) direction. The real (top) and imaginary (bottom) parts of the complex-valued FRF are presented.

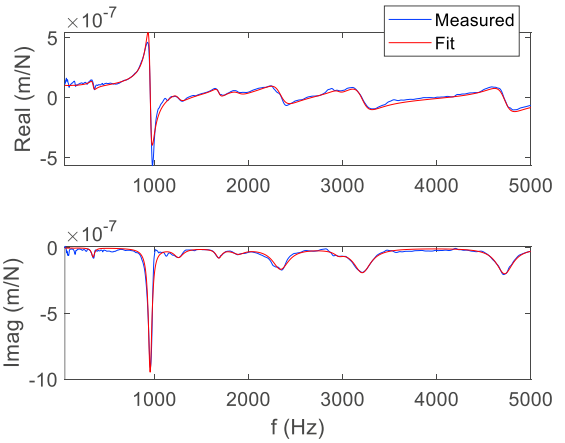

Fig. 15. Tool tip FRF for the y direction. The real (top) and imaginary (bottom) parts of the complex-valued FRF are displayed.

The tool and workpiece frequency response functions, or FRFs, were measured by impact testing, where an instrumented hammer is used to excite the structure and the response is measured using a linear transducer (a low-mass accelerometer for this research); see Figs. 14-15. Modal fitting was applied to extract the modal parameters for the time domain simulation described in Section 3; see Table 2.

Table 2. Tool modal parameters for force measurement setup.

	Tool		
Direction	m (kg)	k (N/m)	c (N-s/m)
x	1779.110	3.95×10^{8}	814240
x	19.221	3.98×10^{7}	12854
x	68.030	5.41×10^{8}	5796
x	17.963	1.76×10^{8}	8251
x	23.032	3.13×10^{8}	8393
x	1.550	5.12×10^{7}	866
x	0.729	3.51×10^{7}	421
x	6.309	5.06×10^{8}	5762
x	10.177	1.32×10^{9}	4956
x	0.327	6.57×10^{7}	450
x	0.185	7.46×10^{7}	274
x	0.164	1.43×10^{8}	193
y	2236.027	5.79×10^{8}	1100218
y	3193.687	2.80×10^{9}	684690
y	27.961	1.35×10^{8}	6715
y	0.617	2.22×10^{7}	177
y	2.507	1.57×10^{8}	1927
y	2.916	3.27×10^{8}	1433
y	2.224	3.16×10^{8}	2273
y	0.324	7.03×10^{7}	430
y	2.348	8.12×10^{8}	1764
y	0.193	7.87×10^{7}	269
y	0.127	1.12×10^{8}	172

The cutting force coefficients for Eqs. 1 and 2 were determined using a linear regression to the measured mean cutting forces over a range of feed per tooth values [1-2]; see Fig. 16. Three measurements were performed at each feed per tooth and a suitable fit was achieved as indicated by the

coefficients of determination, r^2. The same four-component force model was used for all force predictions. The cutting force coefficients for the titanium 6Al-4V (Ti6Al4V) workpiece were: k_{tc} = 1737 N/mm^2, k_{nc} = 224 N/mm^2, k_{te} = 9 N/mm, and k_{ne} = 2 N/mm.

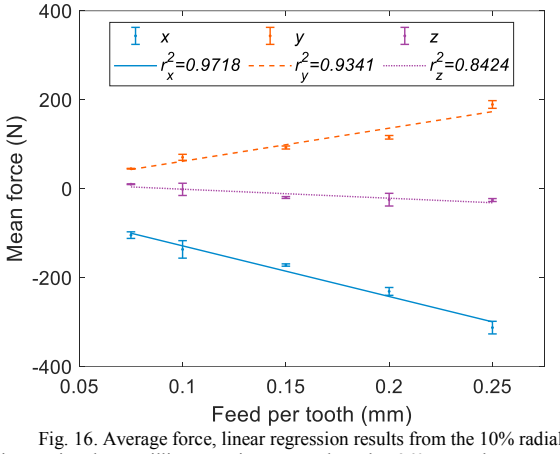

Fig. 16. Average force, linear regression results from the 10% radial immersion down milling experiments conducted at 960 rpm. The mean values and 95% confidence intervals are presented for the range of feed per tooth values.

5. Comparison of measured and simulated forces

The axial depth was held constant at 5 mm and the feed per tooth values were {0.075, 0.100, 0.150, 0.200, and 0.250} mm. Measured and predicted x and y (feed) direction force values for the five manual fits of a single scan are presented for three different feed per tooth values in Figs. 17-19. Reasonable agreement between the measured and simulated forces are observed for all five manual fits with some discrepancies in peak amplitudes. A close examination of the time-dependent force profiles shows that the spacing and duration of the individual teeth engagements vary due to the variable teeth spacing (68-77-72-67-76 deg).

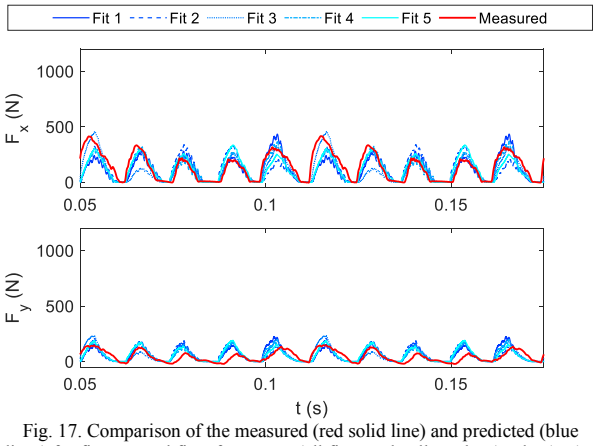

Fig. 17. Comparison of the measured (red solid line) and predicted (blue lines) for five manual fits of one scan (all five teeth, all z values). The (top) x and (bottom) y direction forces are presented; the axial depth is 5 mm and the feed per tooth is 0.075 mm.

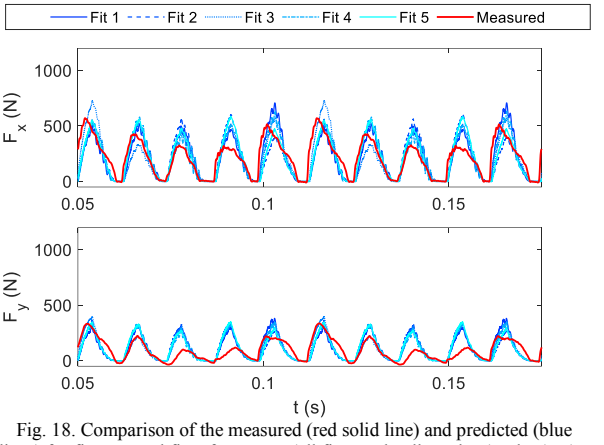

Fig. 18. Comparison of the measured (red solid line) and predicted (blue lines) for five manual fits of one scan (all five teeth, all z values). The (top) x and (bottom) y direction forces are presented; the axial depth is 5 mm and the feed per tooth is 0.150 mm.

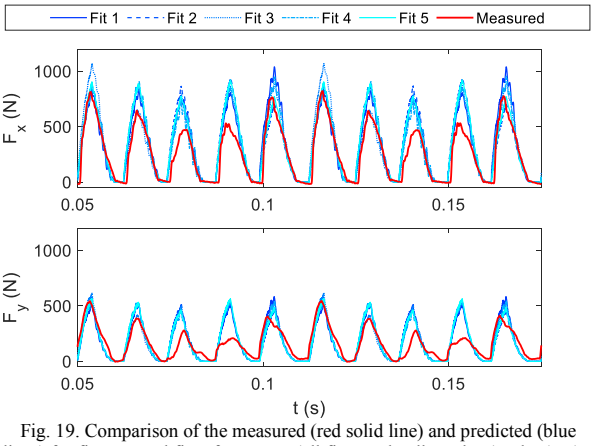

Fig. 19. Comparison of the measured (red solid line) and predicted (blue lines) for five manual fits of one scan (all five teeth, all z values). The (top) x and (bottom) y direction forces are presented; the axial depth is 5 mm and the feed per tooth is 0.250 mm.

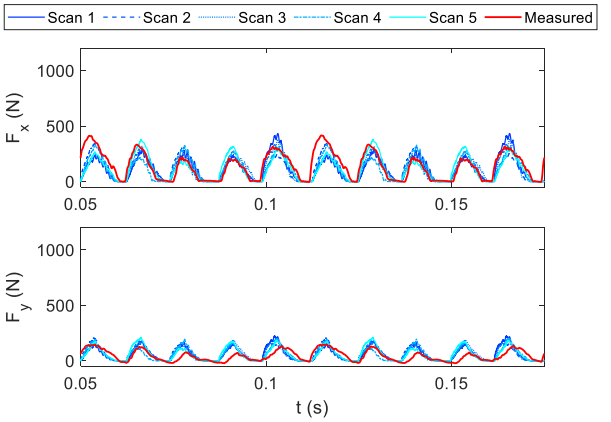

Fig. 20. Comparison of the measured (red solid line) and predicted (blue lines) for the single fits of five scans. The (top) x and (bottom) y direction forces are presented; the axial depth is 5 mm and the feed per tooth is 0.075 mm.

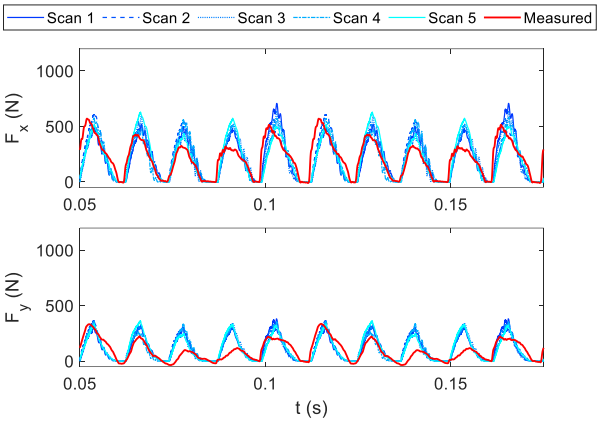

Fig. 21. Comparison of the measured (red solid line) and predicted (blue lines) for the single fits of five scans. The (top) *x* and (bottom) *y* direction forces are presented; the axial depth is 5 mm and the feed per tooth is 0.150 mm.

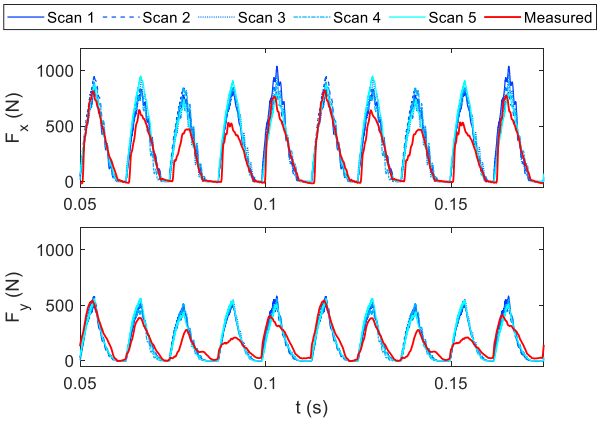

Fig. 22. Comparison of the measured (red solid line) and predicted (blue lines) for the single fits of five scans. The (top) *x* and (bottom) *y* direction forces are presented; the axial depth is 5 mm and the feed per tooth is 0.250 mm.

The measured and predicted *x* and *y* (feed) direction force values for the one manual fit each of five scans are displayed in Figs. 20-22 (same feed per tooth values as Figs. 17-19). Once again, reasonable agreement is observed between the measured and predicted forces with minor discrepancies between the different scanned profiles. As with Fig. 17-19, there are differences between the measured and simulated peak force values. The measurement uncertainty for the cutting edge locations clearly contributes to this disagreement. Even though the uncertainty for five scans (with five associated fits) was shown to be larger than five fits of a single scan in Table 1, Figs. 20-22 are not appreciably different than Figs. 17-19. This suggests that the uncertainty in the cutting edge locations is not the only uncertainty contributor to the predicted force profile.

It is also important to note that the measured force is dependent on the runout in the endmill teeth as mounted in the holder and spindle. Although the *z*-dependent radius of the endmill teeth was identified from the structured light scan, this runout is not necessarily the same as the runout in the force measurement. This is because spindle axis rotation errors, offset between the holder centerline and spindle axis of rotation, and offset between the tool centerline and holder centerline can lead to differences in runout compared to the endmill scan data alone, which was used to model the tool's radius variation as runout in the time domain simulation [1, 24]. This tool-holder-spindle system runout inherently appears in the measured force, but is not necessarily captured in the cutting edge geometry included in the time domain simulation. Additionally, the four force model coefficients obtained from the linear regression to the mean measured cutting force (Fig. 16) contribute uncertainty to the force predictions.

6. Conclusions

To enable advanced digital force modeling for milling, structured light scanning was implemented to measure the cutting edge geometry for a variable pitch endmill. The variation in radius and angle with axial location was measured for two cases to evaluate the measurement uncertainty: 1) a single scan with five manual fits of the single scan; and 2) five scans with a single fit of each scan. Both cases included five manual fits so that the relative contributions of the manual fitting procedure and the scanning process to the measurement uncertainty could be identified. It was found that the uncertainty (standard deviation) was higher with repeated scans, as expected. However, the means of the standard deviations were only 0.005 mm and 0.007 mm for radius and 0.066 deg and 0.092 deg for angle.

A comparison between predicted and measured forces for the two cases did not demonstrate significant differences in levels of agreement. This is attributed to the micrometer-level uncertainties in cutting edge radius and sub-0.1 deg uncertainties in angles. These small variations were not sufficient to strongly influence the predicted time-dependent cutting force. This suggests that structured light scanning is an acceptable metrology system for cutting edge geometry measurement in digital force modeling for milling.

Acknowledgements

The authors gratefully acknowledge financial support from the National Science Foundation (CMMI-1561221). Additionally, this research was supported by the DOE Office of Energy Efficiency and Renewable Energy (EERE), Energy and Transportation Science Division and used resources at the Manufacturing Demonstration Facility, a DOE-EERE User Facility at Oak Ridge National Laboratory.

References

[1] Schmitz, T.L. and Smith, K.S., 2019. Machining Dynamics: Frequency Response to Improved Productivity, 2nd Ed., Springer, New York.
[2] Altintas, Y., 2012. Manufacturing Automation: Metal Cutting Mechanics, Machine Tool Vibrations, and CNC Design, Cambridge University Press.
[3] No, T., Gomez, M., Copenhaver, R., Perez, J.U., Tyler, C. and Schmitz, T.L., 2019. Force and stability modeling for non-standard edge geometry endmills. Journal of Manufacturing Science and Engineering, 141(12).
[4] No, T., Gomez, M., Copenhaver, R., Perez, J.U., Tyler, C. and Schmitz, T.L., 2019. Scanning and modeling for non-standard edge geometry endmills. Procedia Manufacturing, 34, pp.305-315.
[5] Gomez, M., No, T., and Schmitz, T.L., 2020. Digital force prediction for milling. Procedia Manufacturing, 48, pp.873-881.

[6] Gomez, M., No, T., Smith, S., and Schmitz, T.L., 2020. Cutting force and stability prediction for inserted cutters. Procedia Manufacturing, 48, pp.443-451.

[7] Wang, J.J.J. and Yang, C.S., 2003. Angle and frequency domain force models for a roughing end mill with a sinusoidal edge profile. International Journal of Machine Tools and Manufacture, 43(14), pp.1509-1520.

[8] Merdol, S.D. and Altintas, Y., 2004. Mechanics and dynamics of serrated cylindrical and tapered end mills. Journal of Manufacturing Science and Engineering, 126(2), pp.317-326.

[9] Dombóvári, Z., Altintas, Y. and Stépán, G., 2010. The effect of serration on mechanics and stability of milling cutters. International Journal of Machine Tools and Manufacture, 50(6), pp.511-520.

[10]Dombóvári, Z., Munoa, J. and Stépán, G., 2012. General milling stability model for cylindrical tools. Procedia CIRP, 4, pp.90-97.

[11]Stépán, G., Munoa, J., Insperger, T., Surico, M., Bachrathy, D. and Dombóvári, Z., 2014. Cylindrical milling tools: comparative real case study for process stability. CIRP Annals, 63(1), pp.385-388.

[12]Koca, R. and Budak, E., 2013. Optimization of serrated end mills for reduced cutting energy and higher stability. Procedia CIRP, 8, pp.570-575.

[13]Grabowski, R., Denkena, B. and Köhler, J., 2014. Prediction of process forces and stability of end mills with complex geometries. Procedia CIRP, 14, pp.119-124.

[14]Tehranizadeh, F. and Budak, E., 2017. Design of serrated end mills for improved productivity. Procedia CIRP, 58, pp.493-498.

[15]Mahmud, M., Joannic, D., Roy, M., Isheil, A. and Fontaine, J.F., 2011. 3D part inspection path planning of a laser scanner with control on the uncertainty. Computer-Aided Design, 43(4), pp.345-355.

[16]Müller, A., Metzner, S., Hausotte, T., Schubert, D. and Drummer, D., 2019. Separation of locally determined work piece deviations and measurement uncertainties for structured-light scanning of customized polymer gear wheels. AMA Service GmbH, editor, 20, pp.527-534.

[17]Müller, A.M., Schubert, D., Drummer, D. and Hausotte, T., 2020. Determination of the single point uncertainty of customized polymer gear wheels using structured-light scanning with various polygonization settings. Journal of Sensors and Sensor Systems, 9(1), pp.51-60.

[18]Polo, M.E., Cuartero, A. and Felicísimo, Á.M., 2019. Study of uncertainty and repeatability in structured-light 3D scanners. arXiv preprint arXiv:1910.13199.

[19]Adamczyk, M., Kamiński, M., Sitnik, R., Bogdan, A. and Karaszewski, M., 2014. Effect of temperature on calibration quality of structured-light three-dimensional scanners. Applied optics, 53(23), pp.5154-5162.

[20]Kaszynski, A.A., Beck, J.A. and Brown, J.M., 2013. Uncertainties of an automated optical 3d geometry measurement, modeling, and analysis process for mistuned integrally bladed rotor reverse engineering. Journal of Engineering for Gas Turbines and Power, 135(10).

[21]Rosman, G., Rus, D. and Fisher, J.W., 2016. Information-driven adaptive structured-light scanners. In Proceedings of the IEEE Conference on Computer Vision and Pattern Recognition (pp. 874-883).

[22]Jain, S., Allen, A.D. and Zhang, B., 2019, September. Evaluation of the spatial frequency response and the uncertainty for a commercial structured light system. In Applied Optical Metrology III (Vol. 11102, p. 111020X). International Society for Optics and Photonics.

[23]https://www.nist.gov/pml/nist-technical-note-1297.

[24]Schmitz, T.L., Couey, J., Marsh, E., Mauntler, N. and Hughes, D., 2007. Runout effects in milling: Surface finish, surface location error, and stability. International Journal of Machine Tools and Manufacture, *47*(5), pp.841-851.